

Angular-Resolved Optical Characteristics and Threshold Gain Analysis of GaN-Based 2-D Photonics Crystal Surface Emitting Lasers

Shih-Wei Chen^{1,2}, Tien-Chang Lu¹, Ting-Chun Liu¹,
Peng-Hsiang Weng¹, Hao-Chung Kuo¹ and Shing-Chung Wang¹

¹*Department of Photonic and Institute of Electro-Optical Engineering
National Chiao Tung University, Hsinchu*

²*Green Energy & Environment Research Labs
Industrial Technology Research Institute, Hsinchu
Taiwan, R.O.C.*

1. Introduction

Photonic crystal (PhC) surface emitting lasers (PCSELS) utilizing Bragg diffraction mechanism have considerable amounts of publication during the past few years^{1,2,3,4}. Such PhC lasers have many excellent advantages to attract the attention especially in controlling the specific lasing modes such as longitudinal and transverse modes, lasing phenomenon over the large area, and narrow divergence beam. Therefore, we fabricated the GaN-based PCSELS devices with AlN/GaN distributed Bragg reflectors (DBR) and analyzed the PhC laser characteristics caused by the surrounding PhC nanostructure. However, there were many theoretical methods calculating the photonic band diagrams and the distribution of electric or magnetic field of the PhC nanostructure in the past few years, such as 2-D plane wave expansion method (PWEM)^{2,5}, finite difference time domain (FDTD)^{6,7}, transfer matrix method, and multiple scattering method (MSM), etc. Many different advantages and limitations occur while using these methods. Therefore, in our case, we applied the MSM and PWEM to calculate the PhC threshold gain and photonic band diagram by using our PCSEL device structure.

In this chapter, the fabrication process of PhC lasers will be introduced in section 2. They can be divided into two parts, the epitaxial growth and the device fabrication. Section 3 will show the the foudamental mode characteristics of PhC laser, such as laser threshold pumping power, far-field pattern, MSM theoretical calculation methods, and divergence angles. Section 4, in the Bragg diffraction mechanism, each PhC band-edge mode is calculated and exhibits other type of wave coupling mechanism. Section 5, the photinc band diagrams of fundamental and high order lasing modes can be observed by the angular-resolved μ -PL (AR μ -PL) system. Comparing with the theoretical calculation resulted by PWEM and the experiment results of photonic band diagrams measured by AR μ -PL, they can be well matched and show the novel PhC characteristics. Besides, the fundamental and high order PhC lasing modes would be calculated in this section.

2. Fabrication processes

Here, the fabrication processes are composed of two parts. One is the epitaxial growth on sapphire substrates by metal organic chemical vapour deposition (MOCVD), including a 29-pair distributed Bragg reflectors (DBR), a p-GaN layer, multi-quantum wells, a n-GaN, and a un-doped GaN layer, etc. Another one is to fabricate the PhC nanostructure on the epitaxial wafers by the E-beam lithography system and inductive coupled plasma reactive ion etching (ICP-RIE) system. Finally, the GaN-based photonic crystal surface emitting laser (PCSEL) devices with AlN/GaN DBR are performed.

2.1 Growth of nitride-based reflectors and micro-cavity

The detail growth process and experiment parameters of the micro-cavity and nitride-based DBR on sapphire substrates by metal organic chemical vapor deposition (MOCVD) are described as follows:

First, the substrate was thermally cleaned in the hydrogen ambient for 5 min at 1100 °C. And then, a 30 nm-thick GaN nucleation layer was grown at 500°C. The growth temperature was raised up to 1100 °C for the growth of a 2 μm-thick GaN buffer layer. The subsequent epitaxial structure consisted of a 29-pair of quarter-wave AlN/GaN DBR grown at 1100 °C, a 7-lambda cavity ($\lambda = 410$ nm) which includes a 860 nm-thick Si-doped n-GaN layer, 10 pairs In_{0.2}Ga_{0.8}N/GaN (2.5 nm/12.5 nm) MQWs, a 24 nm-thick AlGaIn layer as the electron blocking layer, a 110 nm-thick Mg-doped p-GaN layer, and a 2 nm-thick p⁺ InGaIn layer as the contact layer. The AlN/GaN super-lattices (SL) inserted in the stacks of 29-pair AlN/GaN layers are fabricated because they can release the strain during the growth of AlN/GaN DBR and further improve interface and raise reflectivity of the DBR. Besides, the AlN/GaN DBR can play the role of the low refractive index layer to confine the optical field in the active region in the whole structure. And then, the AlGaIn electron blocking layer was served to reduce the electron overflow to the p-GaN layer. The reflectivity spectrum of the AlN/GaN DBR is shown in Fig. 1. It shows the highest reflectivity of the DBR is about 99% at 416 nm. The stop-band of the DBR is as wide as about 25 nm. Fig. 2. is (a) the OM and (b) cross-sectional TEM images of the as-grown micro-cavity sample.

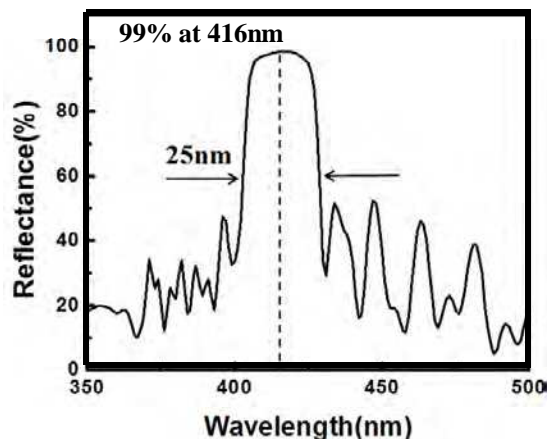


Fig. 1. The reflectivity spectrum of the AlN/GaN

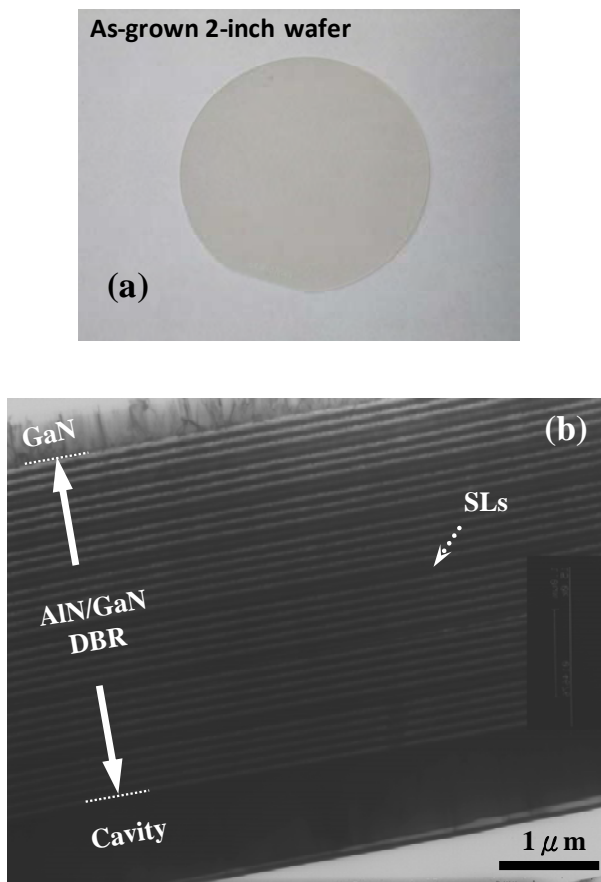


Fig. 2. (a) OM and (b) cross-sectional TEM images of the as-grown micro-cavity sample.

2.2 The fabrication process of photonic crystal surface emitting lasers (PCSELS)

The PhC nanostructure was fabricated on the epitaxial wafers by the following process steps as shown in Fig. 3. In the beginning, the hard mask SiN_x 200 nm was deposited on as-grown samples by PECVD. Then, PMMA layer (150 nm) was spun by spinner and exposed by using E-beam writer to form a soft mask. The pattern on the soft mask was transferred to SiN_x film to form the hard mask by using ICP-RIE (Oxford Plasmalab system 100), and then, the PMMA layer was removed by dipping ACE. The pattern on hard mask was transferred to GaN by using ICP-RIE (SAMCO RIE-101PH) to form the PhC layer. In order to remove the hard mask, the sample is dipped in BOE. Finally, the PCSEL devices have been fabricated as shown in Fig. 4. Fig. 5. shows the plane-view (a) and the cross section (b) of SEM images of our PCSELS. Although the hole profiles of PhC nanostructure etched through the MQWs region are not perfect due to the lateral plasma etching by ICP-RIE shown in Fig. 5(b), the PhC nanostructure near the sample surface which has smooth

etching profile show the largest coupling effects of the light field in the MQW region of about 100nm thickness. Therefore the diffraction profiles of PhC nanostructure still can be observed in the following experiment. Besides, the minimum hole diameter and maximum depth of the PhC nanostructure are about 40nm and 1 μ m, respectively.

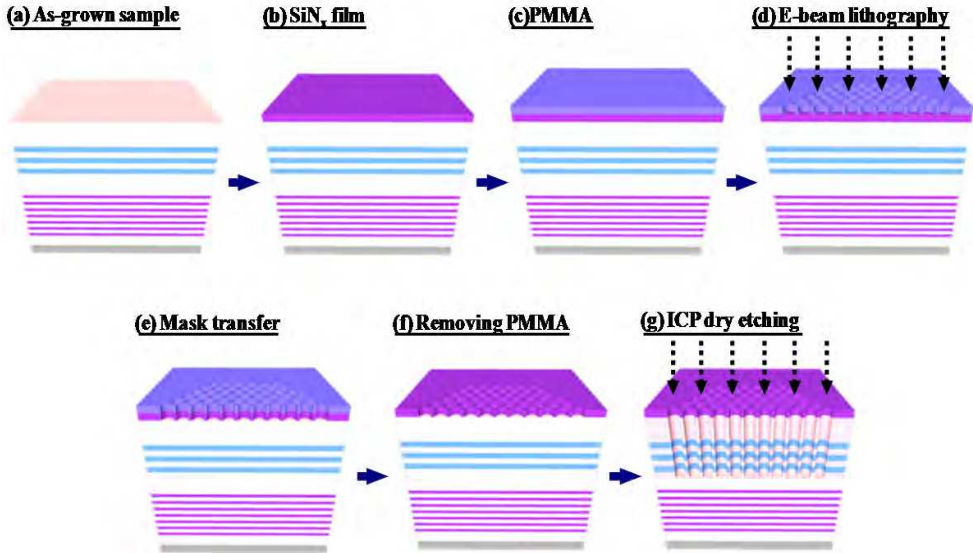


Fig. 3. PCSEL fabrication flowcharts: (a) as-grown sample structure, (b) deposit SiN_x film by PECVD, (c) spin on PMMA, (d) E-beam lithography, (e) PhC pattern transfer to SiN_x layer, (f) remove PMMA by Acetone, and (g) PhC patterns transfer to GaN layer.

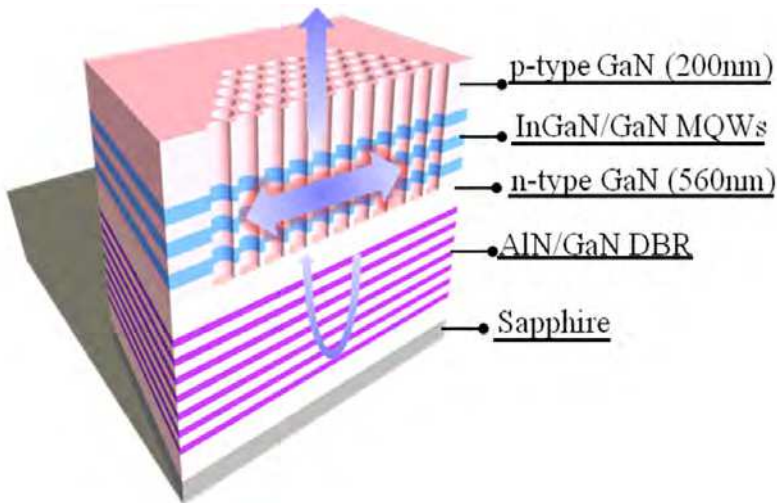


Fig. 4. The GaN-based PCSEL devices with AlN/GaN DBRs

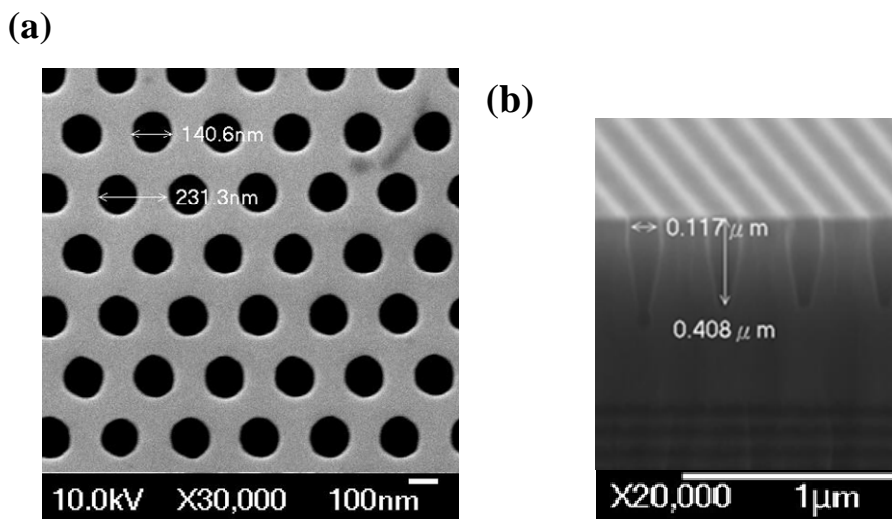


Fig. 5. SEM images of PCSELS: (a) plane view. (b) cross-section view.

3. Optical measurement system and the fundament mode of PhC laser

Section 3.1, the angular-resolved μ -PL (AR μ -PL) system will be introduced, including the pumping lasers, light paths, and so on. Then, using the AR μ -PL system, the characteristics of fundament mode PhC laser would be shown in Section 3.2 and 3.3, such as threshold characteristics and far field patterns, etc. Furthermore, by adopting the multiply scattering method (MSM), the threshold gains of fundamental modes PhC lasers can be calculated in Section 3.4.

3.1 Angular-resolved μ -PL (AR μ -PL)

This section would introduce the angular-resolved μ -PL (AR μ -PL) system which is designed for multiple applications. As shown in Fig. 6, it can observe two optical pump sources, including a frequency tripled Nd:YVO₄ 355 nm pulsed laser with a pulse width of ~ 0.5 ns at a repetition rate of 1 KHz and 325 nm He-Cd continuous wavelength (CW) laser; two optical pump incidence paths, two collecting PL method and two way to collect sample surface image are as well observed. The samples are pumped by the laser beam with an incident angle from 0 degree to 60 degrees normally from the sample. The laser spot size is about 50 μ m in diameter covering the whole PhCs pattern area. The PL spectrum of the samples can be collected by a 15 X objective len and coupled into a spectrometer with a charge-coupled device (Jobin-Yvon iHR320 Spectrometer) or a fiber with a 600 μ m core. The resolution is about 0.07 nm for the spectrometer. Fig. 6. shows the setup of the AR μ -PL system. The GaN-based PCSELS were placed in a cryogenics controlled chamber to perform PL experiment at low temperature. The temperature of the chamber can be controlled from room temperature (300 K) down to 77 K via the liquid nitrogen.

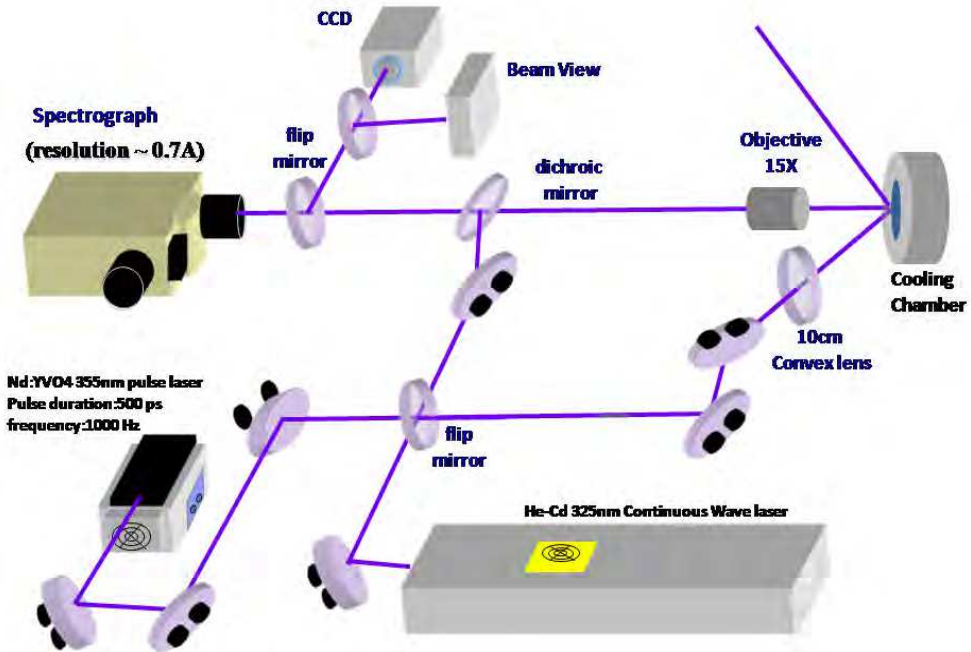


Fig. 6. The angular-resolved μ -PL (AR μ -PL) system

3.2 Threshold characteristics of fundamental mode of PhC lasers

In the optical pumped experiments of PCSEL devices, the lasing action was clearly observed in several devices with different lasing wavelength ranging from 395 nm to 425 nm. Fig. 7 shows the output emission intensity versus the pumping energy density with the PhC lattice constant of about 254 nm. In the figure, the clear threshold pumping energy shows at the threshold pumping energy density of $2.8 \text{ mJ}/\text{cm}^2$, and a peak power density of $5.6 \text{ MW}/\text{cm}^2$. When the laser pumping energy exceeds the threshold energy, the laser output intensity increases abruptly and linearly with the pumping energy. Fig. 8 shows the excitation energy dependent emission spectra of $0.8 E_{\text{th}}$, $1 E_{\text{th}}$, $1.2 E_{\text{th}}$ and $1.3 E_{\text{th}}$. These spectra clearly show the transition behavior from spontaneous emission to stimulated emission. Furthermore, above the threshold, only one dominant peak wavelength of 419.7 nm with a linewidth of 0.19 nm can be observed.

3.3 Far field patterns (FFP) of PhC fundamental mode lasers

The lasing area of the GaN-based 2-D PCSEL, obtained by a CCD camera, is relatively large and covers near the whole area of PhC pattern with only one dominant lasing wavelength as shown in Fig. 9. It's interesting to note that the threshold power density of GaN-based 2-D PCSEL is in the same or even better order than the threshold of the GaN-based VCSEL we have demonstrated recently⁸. Unlike the small emission spots observed in the GaN-based VCSELs, the large-area emission in 2-D PCSEL has great potential in applications and requires high power output operation.

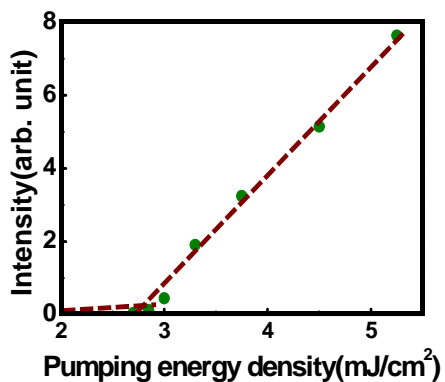


Fig. 7. Laser intensity as a function of pumping energy density

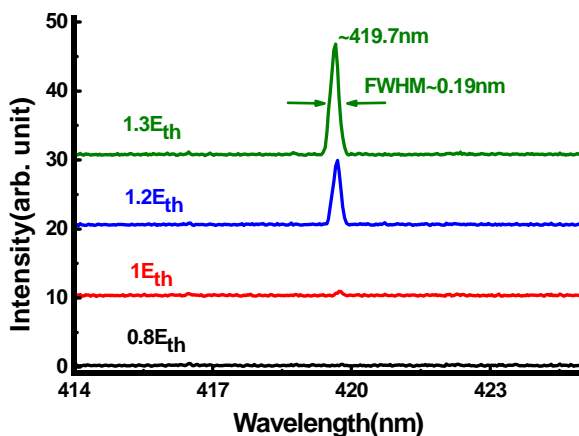


Fig. 8. The lasing spectrums under different pumping energy densities

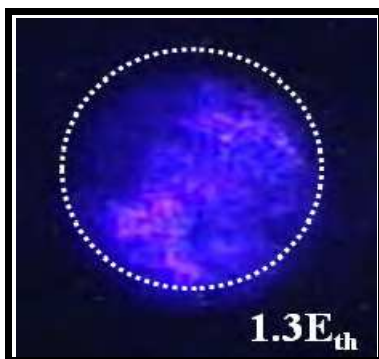


Fig. 9. The lasing CCD image is at 1.3 E_{th} and the dash circle is the PhC nanostructure region of about 50μm

The far-field patterns (FFP) of the laser were detected by an angular-resolved optical pumped system as shown in Fig. 10. In this figure, the lasing far field profiles with different distances from the sample surface were measured. When we increased the measurement distance from the sample surface, the lasing spot splits of four points with two axes, Γ -M and Γ -K directions, indicated that the lasing has strong direction and energy concentration properties in real space. Then, we re-plotted the lasing spot sizes as a function of the measurement distance as shown in Fig. 11. In the figure, it shows the divergence angle of PCSEL determined by the distance of two lasing spot axes of about 5.6 degrees. It is smaller than edge emitting laser ($\sim 10^\circ \sim 20^\circ$) and VCSEL (8°).

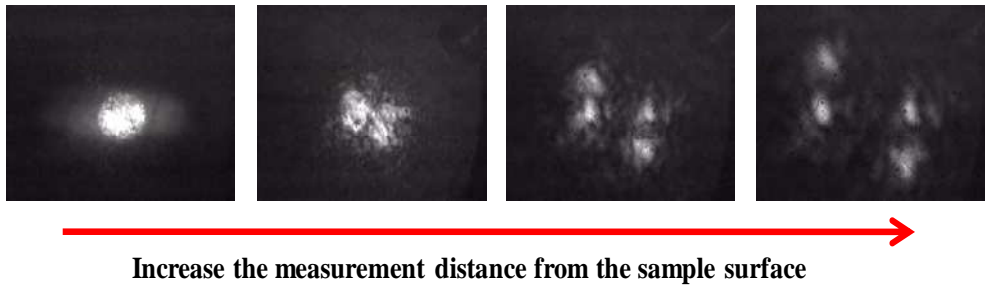


Fig. 10. The far field pattern with different distance from the sample surface collected by objective lens

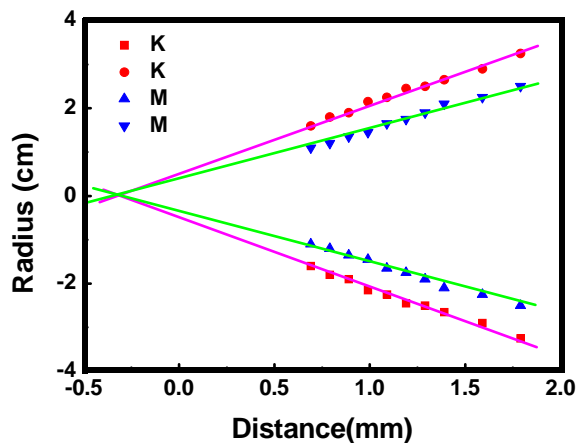


Fig. 11. The divergence angle between the two axes.

3.4 Threshold gain analysis by multiple scattering method (MSM)

This section would introduce the multiple scattering method (MSM) shown below:

The simulation structure is composed of finite two-dimensional PhCs nanostructure with triangular-lattice patterns and parallel cylinders placed in a uniform GaN-based material.

The complex dielectric constant is the light amplification in GaN-based material shown as follows:

$$\epsilon_{background}(\omega) = \epsilon_{GaN}(\omega) - i \frac{2c\sqrt{\epsilon_{GaN}}}{\omega} k_a'' \quad (1)$$

where ϵ_{GaN} represents the dielectric constant varied with frequency of light and k_a'' represents the amplitude gain coefficient of the material. A point source transmitted monochromatic waves are placed at the original point. The total system matrix can be obtained as below⁹:

$$\Gamma_n^i A_n^i - \sum_{j=1}^N \sum_{l \neq i}^{\infty} G_{l,n}^{i,j} A_l^j = T_n^i \quad (2)$$

The A_n^i and T_n^i are matrixes representing expansion coefficients of scattering waves and incident waves, respectively. Here, according to main dipole oscillation in the GaN active region, only the transverse electric (TE) mode polarization (polarization direction perpendicular to the cylinder axis) is considered¹⁰. Eq. (2) could be simplified to an eigen value problem: $MA=T$. If the value of vector A / T is divergent, the laser oscillation condition would be achieved. Therefore, $\det(M)=0$ is the complex determinant equation which is used to search for a pair of variables of threshold amplitude gain k_{am}'' and normalized frequency from $k = \omega/c$ in Eq. (1).

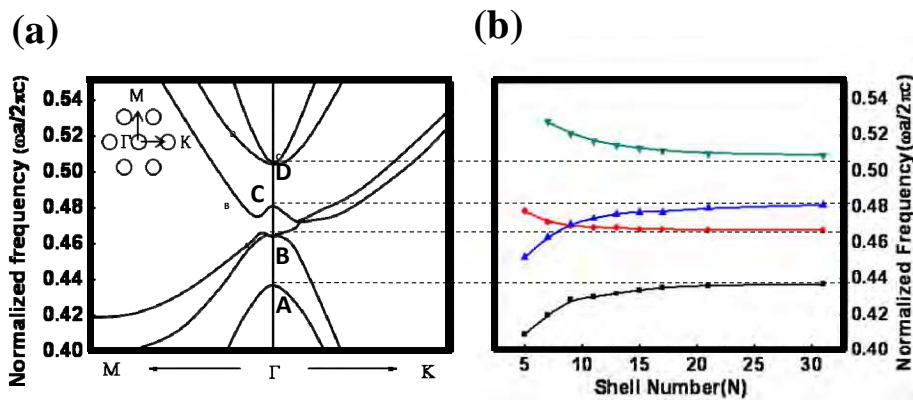


Fig. 12. (a) Photonic band diagram of a PhC triangular lattice with TE mode polarization calculated by PWEM near the first Γ band edges showing four different modes; (b) Normalized frequencies of lasing modes calculated by MSM for different PhC shells (N values).

According to PWEM, the first Γ band edge of photonic band diagram with the PhC triangular lattice and TE mode polarization are calculated as shown in Fig. 12(a). We can find four different band edges causing four resonant modes (A - D) since modes B and D are doubly degenerate. In Fig. 12(b), the normalized frequencies of lasing modes is calculated for different PhC shells (N values) by MSM., where the parameter N is

represented as the number of cylinder layers in the Γ -M direction. The dashed lines of Fig. 12 represent different resonant modes of A, B, C and D at the Γ band edge. It can be observed that the resonant mode frequencies calculated by MSM will approach to band edge frequencies calculated by PWEM when the shell number increases. Therefore, we could obtain more accurate results when the layer number goes beyond 20. Because of the shapes of photonic band diagrams, the blue-shifted or red-shifted trends of normalized frequencies are increased with the shell numbers in Fig. 12(b).

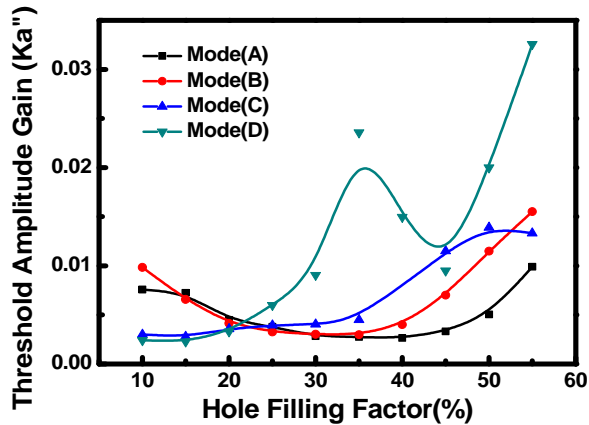


Fig. 13. Threshold amplitude gain of four modes as a function of the hole filling factor. The inset shows the lasing mode at Γ point in the PhC plane using Bragg diffraction scheme¹⁰.

Fig. 13 shows the threshold amplitude gain of modes A-D as a function of the hole filling factor calculated by MSM. The confinement factor and effective refractive index are 0.865 and 2.482 for guided modes in the calculation, respectively. Hence, real parts of ϵ_{GaN} and ϵ_{Hole} are 7.487 and 3.065 for the GaN material and PhC air holes^{11,12}. In the figure, the mode A and B have the lowest threshold gain for hole filling factors of about 35% and 30%; besides, mode C and D have the lowest threshold gain for hole filling factors of about 10% and 15%. This result shows that the proper hole filling factor can control the PhC mode selection.

4. Bragg diffraction mechanism

According to Bragg diffraction theory, the first order Bragg diffraction with 2-D PhC triangular lattice will be introduced in Section 4.1. The high order diffraction mechanism will be shown in Section 4.2 together with K2 and M3 PhC modes.

4.1 First order Bragg diffraction in 2-D PhC triangular lattice^{6,13}

Fig. 14(a) shows a photonic band diagram with PhC triangular lattice. Among the points (A), (B), (C), (D), (E), and (F) in band diagram, each of them presents different lasing modes, including Γ_1 , K2, M1, Γ_2 , K2, and M2, which can control the light propagated in different lasing wavelength and band-edge region. A schematic diagram of the PhC nanostructure in reciprocal space transferred from real space are shown in Fig. 14(b). The parameter of a is

the PhC lattice constant. The K_1 and K_2 are the Bragg vectors with the same magnitude, $|K| = 2\pi/a_0$. Considering the TE modes in the 2-D PhC nanostructure, the diffracted light wave from the PhC structure must satisfy the Bragg's law and energy conservation:

$$k_d = k_i + q_1 K_1 + q_2 K_2, \quad q_{1,2} = 0, \pm 1, \pm 2, \dots \quad (3)$$

$$\omega_d = \omega_i \quad (4)$$

where k_d is a xy-plane wave vector of diffracted light wave; k_i is a xy-plane wave vector of incident light wave; $q_{1,2}$ is order of coupling; ω_d is the frequency of diffracted light wave, and ω_i is the frequency of incident light wave. Eq. (3) represents the momentum conservation, and Eq. (4) represents the energy conservation. When both equations are satisfied, the lasing behavior would be observed.

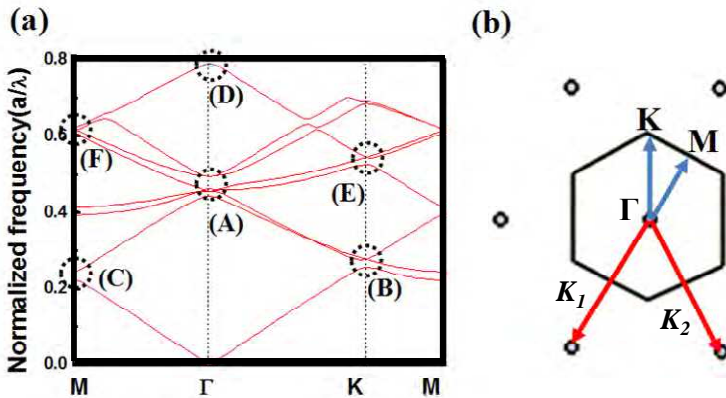


Fig. 14. (a) The band diagram of PhC with triangular lattice; (b) The schematic diagram of PhC with triangular lattice in reciprocal space.

In the calculation, the PhC band-edge lasing behavior would occur at specific points on the Brillouin-zone boundary, including Γ , M , and K which would split and cross. At these PhC lasing band-edge modes, waves propagating in different directions would be coupled and increase the density of state (DOS). Each of these band-edge modes exhibits different types of wave coupling routes. For example, only the coupling at point (C) involves two waves, propagating in the forward and backward directions as shown in Fig. 15(c). In different structures, all of them show similar coupling mechanism but different lasing behaviors. However, they can be divided into six equivalent Γ - M directions. It means that the cavity can exist independently in three different directions to form three independent lasers. Point (B) has a unique coupling characteristic as shown in Fig. 15(b). It forms the triangular shape resonance cavity propagating in three different directions while comparing with the conventional DFB lasers. On the other hand, the point (B) can also be six Γ - K directions in the structure shown two different lasing cavities in different Γ - K directions coexisted independently. In Fig. 15(a) point (A), the coupling waves in in-plane contain six directions of $0^\circ, 60^\circ, 120^\circ, -60^\circ, -120^\circ,$ and 180° . According to the first order Bragg diffraction theory, the coupled light can emit perpendicular from the sample surface as shown in Fig. 16. Therefore, the PhC devices can function as surface emitting lasers.

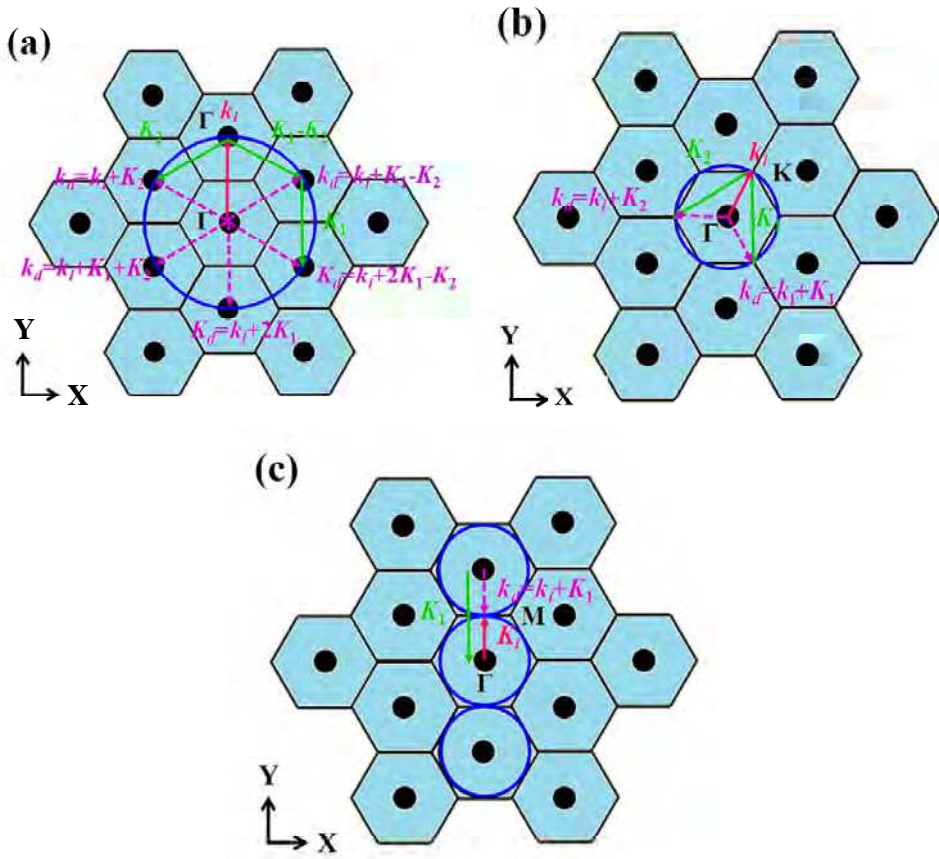


Fig. 15. Wave vector diagram at points (A), (B), (C) in Fig. 13(a); k_i and k_d indicate the incident and diffracted light wave.

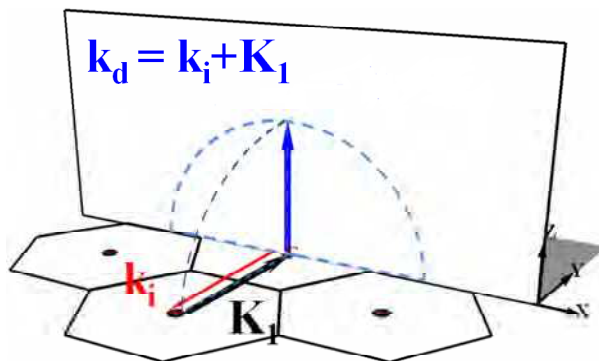


Fig. 16. The wave vector diagram at point (A) in vertical direction.

4.2 High order Bragg diffraction in 2-D PhC with triangular lattice

At point (E) which satisfies the Bragg's law, Fig. 17(a) and (b) show the in-plane and vertical diffraction of the light wave diffracted in three Γ -K directions to three K' points. In the wave-vector diagram of one K' point, the light wave is diffracted to an angle tilted 30° normally from the sample surface as shown in Fig. 17(b). Therefore, the lasing behavior of K2 mode would emit at this specific angle of about 30° .

At point (F), Fig. 18(a) and (b) represented the in-plane and vertical diffraction that the light wave is diffracted in two different Γ -M directions and reaches to three M' points. Fig. 18(b) shows the wave-vector diagram of one M' point where the light wave is diffracted into three independent angles tilted of about 19.47° , 35.26° , and 61.87° normally from the sample surface.

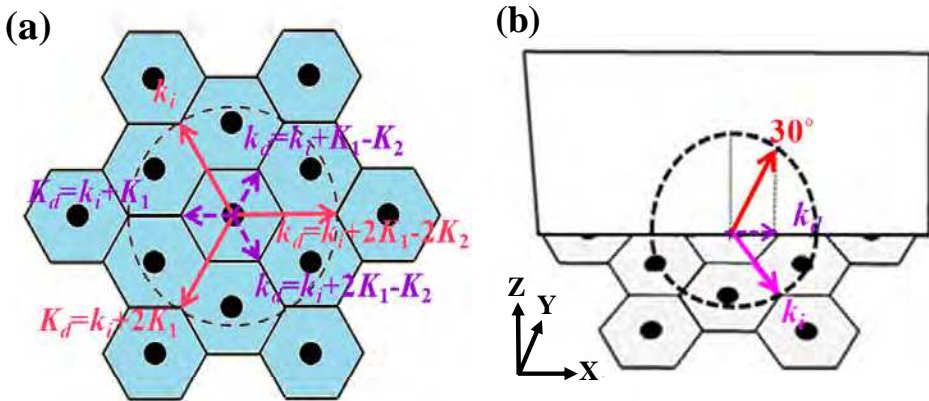


Fig. 17. Wave vector diagram of (a) in-plane and (b) vertical direction at point (E) (or K2 mode); k_i and k_d indicate incident and diffracted light wave.

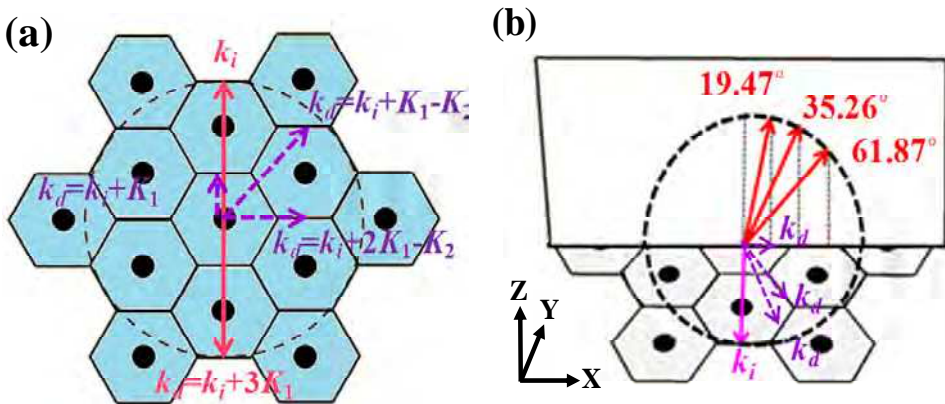


Fig. 18. Wave vector diagram of (a) in-plane and (b) vertical direction at point (F) (or M3 mode); k_i and k_d indicate incident and diffracted light wave.

5. Angular-resolved optical characteristics at different band-edge modes

Section 5.1 shows the transformation method from angular-resolved measurement data to the AR μ -PL diagrams. In Section 5.2, the AR μ -PL diagrams and the divergence angles of Γ_1 , K2, and M3 modes are introduced.

5.1 Data normalization

After measurements by the angular-resolved measurement system, we transformed the AR μ -PL spectrums to obtain the guided modes dispersion relation (reduced frequency $u=\Lambda/\lambda_0$ as y-axis versus in-plane wave vector, $k_{//}$, as x-axis) by the relation $k_{//}=k_0*\sin\theta$. In addition, each wavelength, $I_{PL}(\bar{\theta})$, is normalized relatively to its integrated intensity¹⁴. The normalized AR μ -PL diagram reveals the clear dispersion relation of guided modes and details figures out the relative excitation and out-coupling efficiency.

5.2 AR μ -PL diagram

Pumped by the YVO4 pulse laser and the He-Cd CW laser, the measured dispersion diagrams at Γ_1 mode are observed as shown in Fig. 19. Around Γ_1 mode, the dash lines represent the simulated photonic band diagram by PWEM. The stimulated emission of the lasing phenomenon from the devices provided by the PhC in-plane resonance routes can be observed by a YVO4 pulse laser in Fig. 19(a). The PhC laser shows the vertical emission near the normal direction from the sample surface. However, the diffracted lines in this figure cannot be observed clearly because of high intensity of laser peaks. Thus, the diffracted emissions are measured by a He-Cd CW laser with a lower pumping intensity from the PCSEL devices. Therefore, the diffracted pattern can be observed more clearly in the measured dispersion diagram shown in Fig. 19(b). In this figure, the transverse upward curving lines derived from the Fabry-Perot effect provided by the device structure and modulated by the interference of the DBR layers. The electric field propagating in the PhC structure could be described as a Bloch mode: $E(r) = \Sigma G E_G * \exp [i(k_{//} + G) \cdot r]$ to explain the observed diffraction patterns caused by a PhC nanostructure, where E_G is the electric field component corresponding to harmonic reciprocal lattice vector G , and $k_{//}$ is the in-plane wave vector of the Bloch mode. The reciprocal lattice in K space is a 2-D PhC triangular lattice rotated by 30° with respect to the direct lattice in real space. The reciprocal lattice vectors can be written as: $G = q_1 K_1 + q_2 K_2$, where q_1 and q_2 are integers, and K_1 and K_2 are the two reciprocal lattice basis vectors. Harmonics of the Bloch mode are extracted if their in-plane wave vectors are within the light cone: $|k_{//} + G| < k_0$, where k_0 is defined as $2\pi/a$.

In Fig. 19(b), there are several groups with different slopes of diffraction lines in the dispersion diagram. Different dispersion modes of the diffraction lines with different slopes can be well matched to calculated photonic band diagrams shown as dashed lines by PWEM. The parallel diffraction lines with the same slope represent different guide modes in the in-plane direction. By comparing the Fig. 19(a) with Fig. 19(b), the lasing actually occurs at the third guided mode near the Γ_1 band edge.

In Fig. 20, the measured AR μ -PL diagrams of another PCSEL device with different PhC structure near the K2 modes along the Γ -K direction are measured. By using YVO4 pulse laser pumping, Fig. 20(a) reveals the lasing peaks in the AR μ -PL diagram. Besides, the AR μ -PL diagram is shown in Fig. 20(b) pumped by a CW He-Cd laser. In the figure, the

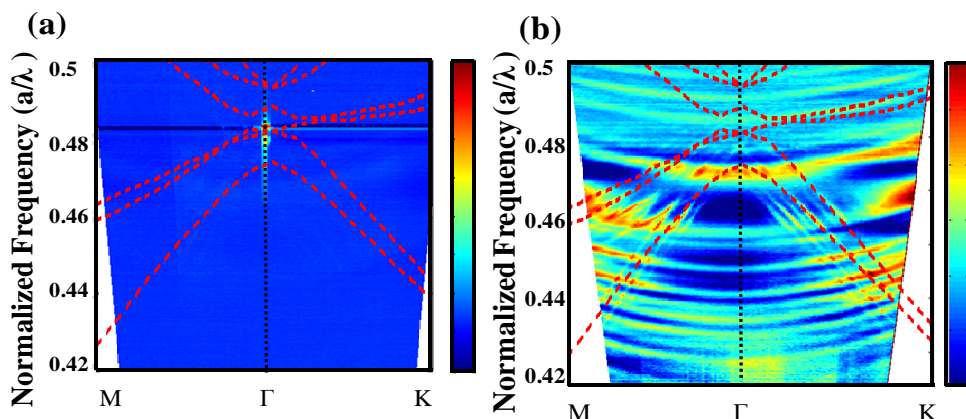


Fig. 19. The measured AR μ -PL diagram near the Γ_1 mode ((a) pumped by YVO4 pulse laser; (b) pumped by He-Cd laser), the dash lines represent the calculated photonic band diagram.

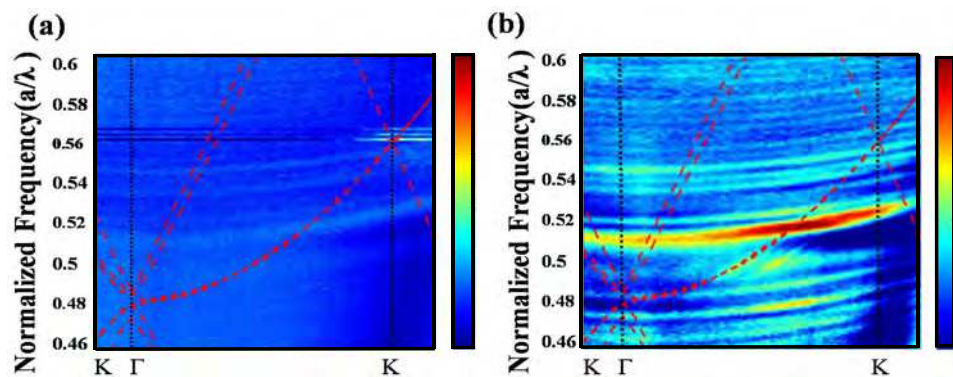


Fig. 20. The measured AR μ -PL diagram near the K2 mode ((a) pumped by YVO4 pulse laser; (b) pumped by He-Cd laser). The dash lines represent the calculated photonic band diagrams.

diffracted lines can be observed and well matched to the calculated 2-D TE-like photonic band diagram, by using parameters of $r/a = 0.285$, $a = 210$ nm, $n_b = 2.560$, $n_a = 2.343$, and $n_{eff} = 2.498$ for calculation shown as the dash lines in Fig. 20. In addition, the experiment results show the lasing beam emission angle of about 29 degree off from the normal along the Γ -K direction, which is exactly matched to the estimated value of about 30 degree derived in the previous section. Furthermore, we measured another PCSEL devices exhibited characteristics of M3 band edge mode along the Γ -M direction. The measured dispersion diagrams pumped by a YVO4 pulse laser and a He-Cd CW laser are shown in Fig. 21(a) and (b), respectively. The lasing peaks can be clearly seen in Fig. 21(a). The diffracted patterns can be observed in Fig. 21(b) and well matched by using parameters of $r/a = 0.204$, $a = 230$ nm, $n_b = 2.617$, $n_a = 1.767$, and $n_{eff} = 2.498$. Shown as the dash lines in Fig. 21, the emission angle of lasing beam was about 59.5 degree off from the normal along the Γ -K direction, which was also quite matched to one of the estimated values of about 61.87

degree derived in the previous section. The reason that only one emission angle was obtained could be due to the fact that we only measured the AR μ -PL diagram along one Γ -M direction.

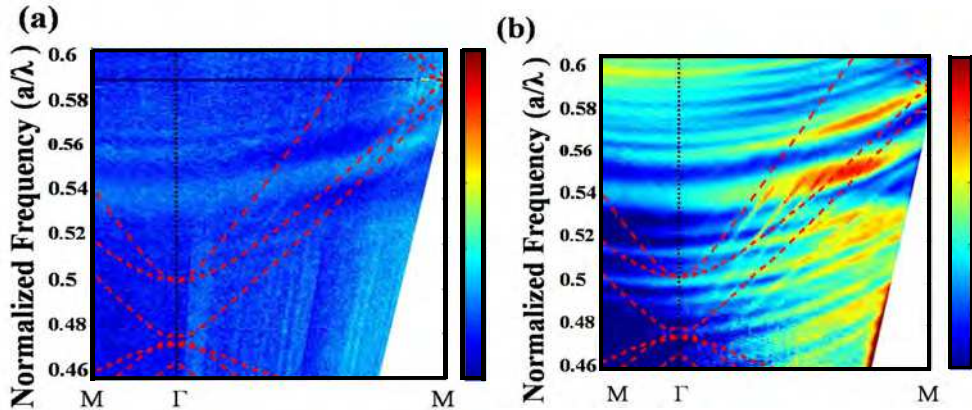


Fig. 21. The measured AR μ -PL diagram near the M3 mode ((a) pumped by YVO4 pulse laser; (b) pumped by He-Cd laser). The dash lines represent the calculated photonic band diagrams.

Each of PhC band-edge modes exhibited specific emission angle by different type of wave coupling mechanism in Fig. 19(a), Fig. 20(a), and Fig. 21(a). Finally, Fig. 22 shows the divergence angles of Γ 1, K2, and M3 band-edge modes on the normal plane from the sample surface. The lasing emission angles are about 0° , 29° , and 59.5° , and the divergence angles of laser beams are about 1.2° , 2.5° , and 2.2° for (Γ 1, K2, and M3) band edge modes, respectively. Due to the alignment difficulties in the AR μ -PL system, the measured emission angles might have some offset values of about 1° to 2° .

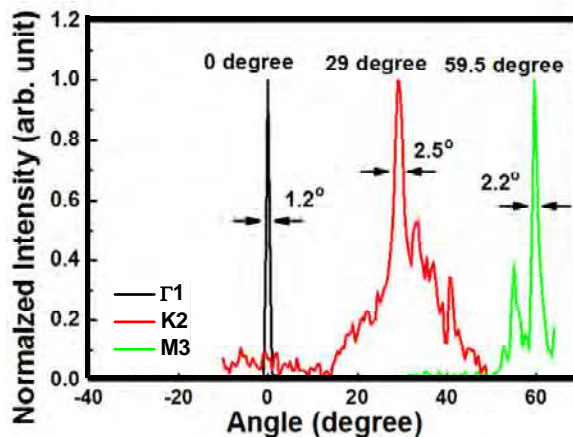


Fig. 22. The emission angles and divergence angles of Γ 1, K2, and M3 band-edge modes on the normal plane from the sample surface.

6. Conclusion

In the chapter, the optical pumped of GaN-based 2-D photonic crystal surface emitting lasers (PCSELS) with AlN/GaN distributed Bragg reflectors (DBR) are fabricated and measured. The laser has a 29-pair bottom DBR which plays the role of a low refractive index layer to enhance the coupling between photonic crystal (PhC) nanostructure and electrical field in the whole cavity. Therefore, the lasing action can be achieved in the optical pumping system. Each of these laser devices emits only one dominant wavelength between 395 nm and 425 nm. That normalized frequency of PhC lasing wavelength can be well matched to these three band-edge frequencies (Γ_1 , K2, M3) indicated that the lasing action can only occur at specific band-edges. In the angular-resolved μ -PL (AR μ -PL) system, the diffracted lines in the AR μ -PL diagrams of PCSEL devices can be further matched to the calculated 2-D TE-like photonic band diagram calculated by PWEM. These three band-edge frequencies (Γ_1 , K2, M3) have different emission angles in the normal direction of about 0° , 29° , and 59.5° and are further confirmed by the Bragg theory. The divergence angles of the (Γ_1 , K2, M3) modes are about 1.2° , 2.5° , and 2.2° . Moreover, according to multiple scattering method (MSM), the resonant mode frequencies will approach to band edge frequencies compared with plane wave expansion method (PWEM). In addition, the threshold gain of four resonant modes varies with the filling factor. This result shows that the proper hole filling factor can control the PhC mode selection. Finally, all of these calculation and experiment results indicate that GaN-based PCSELS could be a highly potential optoelectronic device for lasers in the next generation.

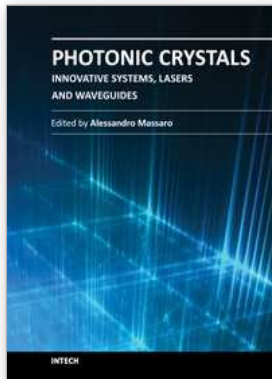
7. Acknowledgment

The authors would like to gratefully acknowledge A. E. Siegman at Stanford for his fruitful suggestion. The study was supported by the MOE ATU program, Nano Facility Center and, in part, by the National Science Council in Taiwan

8. References

- [1] Imada, M.; Noda, S.; Chutinan, A.; Tokuda, T.; Murata, M. & Sasaki, G. Coherent two-dimensional lasing action in surface-emitting laser with triangular-lattice photonic crystal structure. *Applied Physics Letters*, Vol. 75, (1999), pp. 316-318, ISSN 0003-6951.
- [2] Noda, S.; Yokoyama, M.; Imada, M.; Chutinan, A. & Mochizuki, M. Polarization Mode Control of Two-Dimensional Photonic Crystal Laser by Unit Cell Structure Design. *Science*, Vol. 293, (2001), pp. 1123-1125, ISSN 0036-8075.
- [3] Ryu, H. Y.; Kwon, S. H.; Lee, Y. J. & Kim, J. S. Very-low-threshold photonic band-edge lasers from free-standing triangular photonic crystal slabs. *Applied Physics Letters*, Vol. 80, (2002), pp. 3476-3478, ISSN 0003-6951.
- [4] Turnbull, G. A.; Andrew, P.; Barns, W. L. & Samuel, I. D. W. Operating characteristics of a semiconducting polymer laser pumped by a microchip laser. *Applied Physics Letters*, Vol. 82, (2003), pp. 313-315, ISSN 0003-6951.
- [5] Sakai, K.; Miyai, E.; Sakaguchi, T.; Ohnishi, D.; Okano, T. & Noda, S. Lasing band-edge identification for a surface-emitting photonic crystal laser. *IEEE Journal on Selected Areas in Communications*, Vol. 23, (2005), pp. 1335-1340, ISSN 0733-8716.

- [6] Imada, M.; Chutinan, A.; Noda S. & Mochizuki M. Multidirectionally distributed feedback photonic crystal lasers. *Physical Review B*, Vol. 65, (2002), pp. 195306, ISSN 1098-0121.
- [7] Yokoyama M. & Noda S. Finite-difference time-domain simulation of two-dimensional photonic crystal surface-emitting laser. *Optics Express*, Vol. 13, (2005), pp. 2869-2880, ISSN 1094-4087.
- [8] Wang, S. C.; Lu, T. C.; Kao, C. C.; Chu, J. T.; Huang, G. S.; Kuo, H. C.; Chen, S. W.; Kao, T. T.; Chen, J. R. & Lin, L. F. Optically Pumped GaN-based Vertical Cavity Surface Emitting Lasers: Technology and Characteristics. *Japanese Journal of Applied Physics*, Vol. 46, (2007), pp. 5397-5407, ISSN 0021-4922.
- [9] Nojima, S. Theoretical analysis of feedback mechanisms of two-dimensional finite-sized photonic-crystal lasers. *Journal of Applied Physics*, Vol. 98, (2005), pp. 043102, ISSN 0021-8979.
- [10] Lu, T. C.; Chen, S. W.; Lin, L. F.; Kao, T. T.; Kao, C. C.; Yu, P.; Kuo, H. C.; Wang, S. C. & Fan, S. H. GaN-based two-dimensional surface-emitting photonic crystal lasers with AlN/GaN distributed Bragg reflector. *Applied Physics Letters*, Vol. 92, (2008), pp. 011129, ISSN 0003-6951.
- [11] Chen, S. W.; Lu, T. C.; Hou, Y. J.; Liu, T. C.; Kuo H. C. & Wang, S. C. Lasing characteristics at different band edges in GaN photonic crystal surface emitting lasers. *Applied Physics Letters*, Vol. 96, (2010), pp. 071108, ISSN 0003-6951.
- [12] Chen Y. Y. & Ye, Z. Propagation inhibition and wave localization in a two-dimensional random liquid medium. *Physical Review E*, Vol. 65, (2002), pp. 056612, ISSN 1539-3755.
- [13] Notomi, M.; Suzuki, H. & Tamamura, T. Directional lasing oscillation of two-dimensional organic photonic crystal lasers at several photonic band gaps. *Applied Physics Letters*, Vol. 78, (2001), pp. 1325-1327, ISSN 0003-6951.
- [14] Soller, B. J.; Stuart, H. R. & Hall, D. G. Energy transfer at optical frequencies to silicon-on-insulator structures. *Optics Letters*, Vol. 26, (2001), pp. 1421-1423, ISSN 0146-9592.



Photonic Crystals - Innovative Systems, Lasers and Waveguides

Edited by Dr. Alessandro Massaro

ISBN 978-953-51-0416-2

Hard cover, 348 pages

Publisher InTech

Published online 30, March, 2012

Published in print edition March, 2012

The second volume of the book concerns the characterization approach of photonic crystals, photonic crystal lasers, photonic crystal waveguides and plasmonics including the introduction of innovative systems and materials. Photonic crystal materials promises to enable all-optical computer circuits and could also be used to make ultra low-power light sources. Researchers have studied lasers from microscopic cavities in photonic crystals that act as reflectors to intensify the collisions between photons and atoms that lead to lasing, but these lasers have been optically-pumped, meaning they are driven by other lasers. Moreover, the physical principles behind the phenomenon of slow light in photonic crystal waveguides, as well as their practical limitations, are discussed. This includes the nature of slow light propagation, its bandwidth limitation, coupling of modes and particular kind terminating photonic crystals with metal surfaces allowing to propagate in surface plasmon-polariton waves. The goal of the second volume is to provide an overview about the listed issues.

How to reference

In order to correctly reference this scholarly work, feel free to copy and paste the following:

Shih-Wei Chen, Tien-Chang Lu, Ting-Chun Liu, Peng-Hsiang Weng, Hao-Chung Kuo and Shing-Chung Wang (2012). Angular-Resolved Optical Characteristics and Threshold Gain Analysis of GaN-Based 2-D Photonics Crystal Surface Emitting Lasers, Photonic Crystals - Innovative Systems, Lasers and Waveguides, Dr. Alessandro Massaro (Ed.), ISBN: 978-953-51-0416-2, InTech, Available from: <http://www.intechopen.com/books/photonic-crystals-innovative-systems-lasers-and-waveguides/angular-resolved-optical-characteristics-and-threshold-gain-analysis-of-gan-based-2-d-photonics-crys>

INTECH
open science | open minds

InTech Europe

University Campus STeP Ri
Slavka Krautzeka 83/A
51000 Rijeka, Croatia
Phone: +385 (51) 770 447
Fax: +385 (51) 686 166
www.intechopen.com

InTech China

Unit 405, Office Block, Hotel Equatorial Shanghai
No.65, Yan An Road (West), Shanghai, 200040, China
中国上海市延安西路65号上海国际贵都大饭店办公楼405单元
Phone: +86-21-62489820
Fax: +86-21-62489821

© 2012 The Author(s). Licensee IntechOpen. This is an open access article distributed under the terms of the [Creative Commons Attribution 3.0 License](#), which permits unrestricted use, distribution, and reproduction in any medium, provided the original work is properly cited.